Electronic structure of hydrogenated diamond: Microscopical insight into surface conductivity

S. Iacobucci,[1,*] Paola Alippi,[2,†] P. Calvani,[2] M. Girolami,[2] F. Offi,[3] L. Petaccia,[4] and D. M. Trucchi[2]

[1]*CNR-ISM, Istituto di Struttura della Materia del Consiglio Nazionale delle Ricerche, c/o Dipartimento di Scienze Università di Roma Tre, Via della Vasca Navale 84, 00146 Rome, Italy*

[2]*CNR-ISM, Istituto di Struttura della Materia del Consiglio Nazionale delle Ricerche, Via Salaria, Km 29.300, I-00016 Monterotondo Scalo, Rome, Italy*

[3]*Dipartimento di Scienze, Università Roma Tre, via della Vasca Navale 84, 00146 Rome, Italy*

[4]*Elettra Sincrotrone Trieste, Strada Statale 14 km 163.5, I-34149 Trieste, Italy*

(Received 25 November 2015; revised manuscript received 30 May 2016; published 18 July 2016)

We have correlated the surface conductivity of hydrogen-terminated diamond to the electronic structure in the Fermi region. Significant density of electronic states (DOS) in proximity of the Fermi edge has been measured by photoelectron spectroscopy (PES) on surfaces exposed to air, corresponding to a *p*-type electric conductive regime, while upon annealing a depletion of the DOS has been achieved, resembling the diamond insulating state. The surface and subsurface electronic structure has been determined, exploiting the different probing depths of PES applied in a photon energy range between 7 and 31 eV. *Ab initio* density functional calculations including surface charge depletion and band-bending effects favorably compare with electronic states measured by angular-resolved photoelectron spectroscopy. Such states are organized in the energy-momentum space in a twofold structure: one, bulk-derived, band disperses in the Γ-X direction with an average hole effective mass of $(0.43 \pm 0.02)m_0$, where m_0 is the bare electron mass; a second flatter band, with an effective mass of $(2.2 \pm 0.9)m_0$, proves that a hole gas confined in the topmost layers is responsible for the conductivity of the (2×1) hydrogen-terminated diamond (100) surface.

DOI: 10.1103/PhysRevB.94.045307

Surface properties of matter, while investigated for decades, are still an elusive field of research, where the discovery of new phenomena goes hand in hand with continuous efforts to solve old issues. For example, the characterization of insulating materials hosting topological conductive surfaces, the so-called "topological insulators," is nowadays a new and fashionable scientific topic [1], but still synthetic coating of surfaces is also being investigated [2], excitons at metal surfaces have finally been successfully probed [3], and new evidence of the diversity of magnetic phenomena at surfaces has also been reported [4]. A paradigmatic example of a well-known phenomenon still awaiting to be fully characterized and explained in detail is the surface conductivity of diamond. Diamond is characterized as an incomparable material for a wide range of applications. Its mechanical, thermal, and electronic properties [5] have been already exploited for biological and chemical sensing [6], thermionic emitters [7], and, recently, also solar absorbers [8]. Although intrinsic diamond is an insulator, it is well known that hydrogen-terminated diamond (HD) surfaces exposed to air exhibit surface *p*-type conductivity [9]. Such excellent electric conductivity is a very attractive property for high-power and high-frequency applications [10].

According to the currently accepted model [9,11–13], the huge increase of HD surface conductance (up to 7 orders of magnitude) is a combined effect of hydrogen termination and atmospheric layer adsorption. Indeed, HD negative electron affinity due to hydrogen termination promotes electron transfer from diamond valence bands into empty acceptor levels of surface adsorbates; this in turn induces an upward bending of the electronic bands at the surface and the formation of a quasi-two-dimensional (2D) hole channel nested a few nanometers below it, as recently proven by a low-temperature characterization of diamond in-plane gated field-effect transistors [14].

A large number of both technological and fundamental studies have highlighted the correlation between enhanced HD surface conductivity and the adsorption of a molecular layer [13,15–17]. However, an accurate ascertainment of the HD electronic structure is still missing, despite its pivotal role for the full technological exploitation of this intriguing phenomenon [18]. Moreover, while a detailed determination of the Fermi surface has been recently provided in the case of heavily doped bulk diamond [19], little is known on the 2D hole band forming at the surface of hydrogenated diamond.

In this work, we determine the electronic structure close to the Fermi energy of both the surface and the subsurface region of air-exposed HD by angular-resolved photoemission spectroscopy (ARPES) on samples that were structurally and electrically characterized by low-energy electron diffraction (LEED) and conductivity measurements, respectively. We rely on ARPES different information depths at photon energies ($h\nu$) of 7 eV and 31 eV [20]. In the case of a conductive oxide, it has already been shown [21] that low-energy ARPES is a very effective tool to determine the band structure of a 2D electron gas nested below the Fermi level and caused by a charge accumulation layer: in fact, adequate subsurface sensitivity is allowed by the increased depth of low-energy electrons [22]. ARPES data are compared with density functional theory (DFT) band structure calculations, performed within the projector augmented wave method (PAW) [23] and the Perdew-Burke-Ernzerhof (PBE) [24] approximation for the exchange-correlation potential, as implemented in the Vienna Ab initio Simulation Package (VASP) [25].

*stefano.iacobucci@cnr.it
†paola.alippi@cnr.it

Single-crystal (001) diamond plates, with boron concentration of 5×10^{15} cm^{-3}, have been used. Sample surfaces, with nominal roughness of less than 30 nm, have been cleaned according to standard protocols [26] and hydrogenated in a microwave chemical vapor deposition (CVD) system. The electrical conductance G has been measured by means of a two-point probe method. Immediately after sample removal from the CVD chamber, $G_{\mathrm{ANN}} \simeq 10^{-12}\ \Omega^{-1}$ has been registered at room temperature, increasing upon exposure to air for 12 h up to $G_{\mathrm{AIR}} \simeq 10^{-5}\ \Omega^{-1}$. The initial G_{ANN} value has been recovered by annealing the samples in a vacuum chamber at 670 K for 1 h. The reversibility of the switch from a high- to low-conductivity regime has been verified by repeating the electrical measurements after a new exposure to air and subsequent annealing steps. These findings, while resembling the results of Maier *et al.* [9], established a reliable procedure that we employed to correlate macroscopic electrical characteristics of conductive (AIR) and insulating (ANN) regimes to corresponding microscopic features of the electronic structure measured by photoemission spectroscopy (PES).

PES experiments have been performed at the BaDElPh beam line [27] of the Elettra Synchrotron (Trieste) by detecting the photoelectron polar angular distribution within a cone of $\pm 13^{\circ}$ around the Γ-X direction and an angular resolution of about 0.25°. To determine the Fermi level position (E_{F}) and the experimental energy resolution ($\simeq$ 100 meV), a sputtered polycrystal Cu surface has been used.

Angle-integrated PES spectra of a HD sample, measured at room temperature, are displayed in Fig. 1(a), after air exposition (AIR, red squares) and thermal annealing (ANN, black squares). Average data filters (black lines) have been applied on the ANN spectra to smooth the experimental noise. ANN data are recorded from a very lightly doped sample; as such, it may be expected that samples may become charged, thus compromising the ability to determine the binding energy of any data. To achieve a control on the binding energy position, spectra have been systematically recorded while varying the position of the photon spot, i.e., as a function of the distance between the photon spot and a metal ring used to ground the sample itself: by registering the energy variation of the spectral features as a function of this distance, we could retrieve the right binding energy positions. Furthermore, in order to minimize sample charging, the incident photon flux has been reduced. Hence, much lower intensity is measured on ANN samples with respect to AIR ones, and the resulting poor statistics prevented us from acquiring ARPES data. In this respect, although the acquisition has been limited to integrated spectra, some valuable differential information between ANN and AIR samples has been achieved and highlighted through the discussion of Fig. 1.

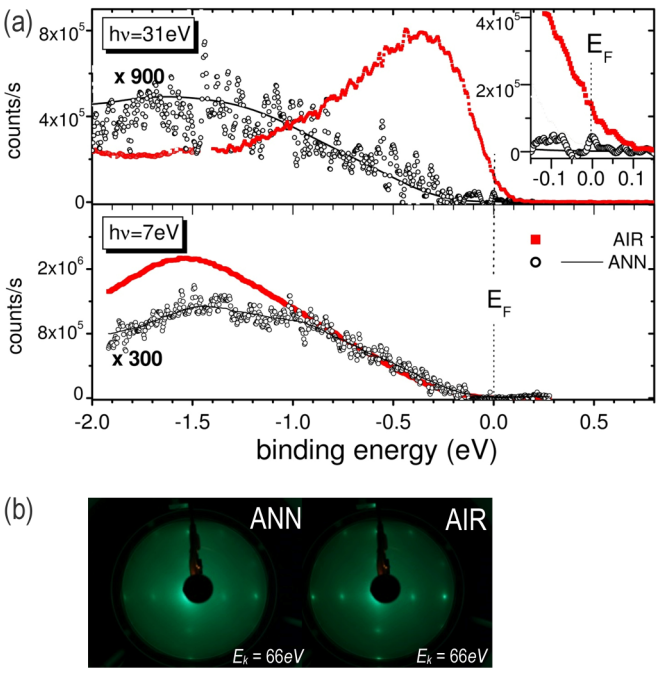

FIG. 1. (a) Angle-integrated PES spectra of the air-exposed (AIR, red squares) and the UHV-annealed (ANN, black squares) HD sample, measured at $h\nu = 31$ eV and $h\nu = 7$ eV. Black lines are amplified data averages of the ANN sample spectra. A magnification of the Fermi-level region is shown in the inset. (b) LEED pattern of the $(2 \times 1)(100)$ surface after ANN and AIR treatments.

For $h\nu = 31$ eV, the ANN spectrum shows vanishing intensity close to E_{F} (binding energy, BE, $= 0$ eV) even upon an amplification by a factor 900. By contrast, after air exposition, significant PES intensity crossing E_{F} is detectable, as evident from the enlarged BE region shown in the inset. The AIR spectrum is also characterized by a pronounced bump at BE $\simeq -0.3$ eV. These spectroscopical results are in line with the electrical characteristics of the corresponding conductivity measurements. In fact, as the PES intensity roughly reflects the one-electron DOS, the nonvanishing value at E_{F} is a microscopical imprinting of the conductive state of air-exposed samples.

To probe the electronic structure stemming from states deeper from the surface of the HD sample, PES spectra have been measured at $h\nu = 7$ eV, exploiting the expected larger photoelectron information depth of slow electrons [21]. The vanishing intensity close to E_{F} is a common finding for the ANN and the AIR samples, in line with the nonconductive regime characteristic of bulk diamond. Although the interpretation of spectral features at low $h\nu = 7$ eV is not straightforward, this similarity points out that air exposure has no detectable effect on the subsurface electronic states. Furthermore, similar shapes of the high- and low-energy spectra in the ANN samples support the correlation between their electronic structures and the insulating state. In AIR samples, instead, the nonvanishing DOS close to E_{F} evident in the $h\nu = 31$ eV excited spectrum is at variance with $h\nu = 7$ eV: the comparison between the two probing depths ($\gg 10$ nm and $\simeq 1$ nm, respectively) [20] points out that changes on the electronic structure induced by air exposure are limited within the few topmost layers under the HD surface.

PES results can be interpreted within the currently accepted model of HD conductivity [13], thereby strengthening the correlation between the conductive/insulating behavior of HD sample and the adsorption/desorption of a molecular layer. In fact, (i) in AIR conducting samples, nonzero DOS in the vicinity of E_{F} is compatible with partially occupied electronic bands and hole carrier formation induced by charge transfer from the HD surface to an adsorbed molecular layer; (ii) spectra taken at different photon energies testify to the

confinement of the conductive electronic states within a few layers under the surface, thus corroborating the band-bending picture; (iii) in ANN samples, occupied states of the diamond valence band lie well below E_F, since the annealing process removes the molecular layers adsorbed on the surface during air exposure and brings back the insulating behavior.

We mention here that we registered spectral variations—the main of which is an energy drift of the whole spectrum toward deeper BEs—as a function of the acquisition time, reasonably due to the photon beam interaction with the adsorbed surface layer. These findings resemble the results of Nebel *et al.* [28], who reported irreproducible signals in scanning tunneling microscopy measurements on HD samples in solution, and they are an indication of the weakness of the bonding between the adsorbed layer and the HD surface. Reasonably, they are the ultimate effects of the interaction with the photon beam, which results in charging effects produced by a reduction of the adsorbed layer. Nevertheless, by reducing the photon flux, we were able to minimize such effects and derive the energy position of the spectrum of the AIR sample.

The impact of molecular adsorption on the crystallographic order at the HD surface samples has been analyzed throughout LEED measurements. In Fig. 1(b), sharp diffraction patterns with the (2×1) reconstruction characteristic of the (100) HD surface [29] are clearly visible at 66 eV of electron energy. We remark here that they are detectable in both the insulating ANN state and in the conductive AIR state, the lower quality of the diffraction pattern in the ANN sample likely being due to charging effects. The persistence of the (2×1) LEED pattern after air exposure, besides testifying that the adsorbed layer does not affect the surface long-range order, also suggests that the H passivation prevents significant contamination. (A very thin and/or possibly incomplete molecular coverage might be argued.)

Without specifying the molecular species responsible for the charge transfer from HD electronic bands, we solved the DFT-PBE ground state of a model system where a surface density of fictitious H atoms with fractional charge mimes an H-terminated diamond surface that is partially depleted of electrons. In particular, we use a (2×1), [001]-oriented,

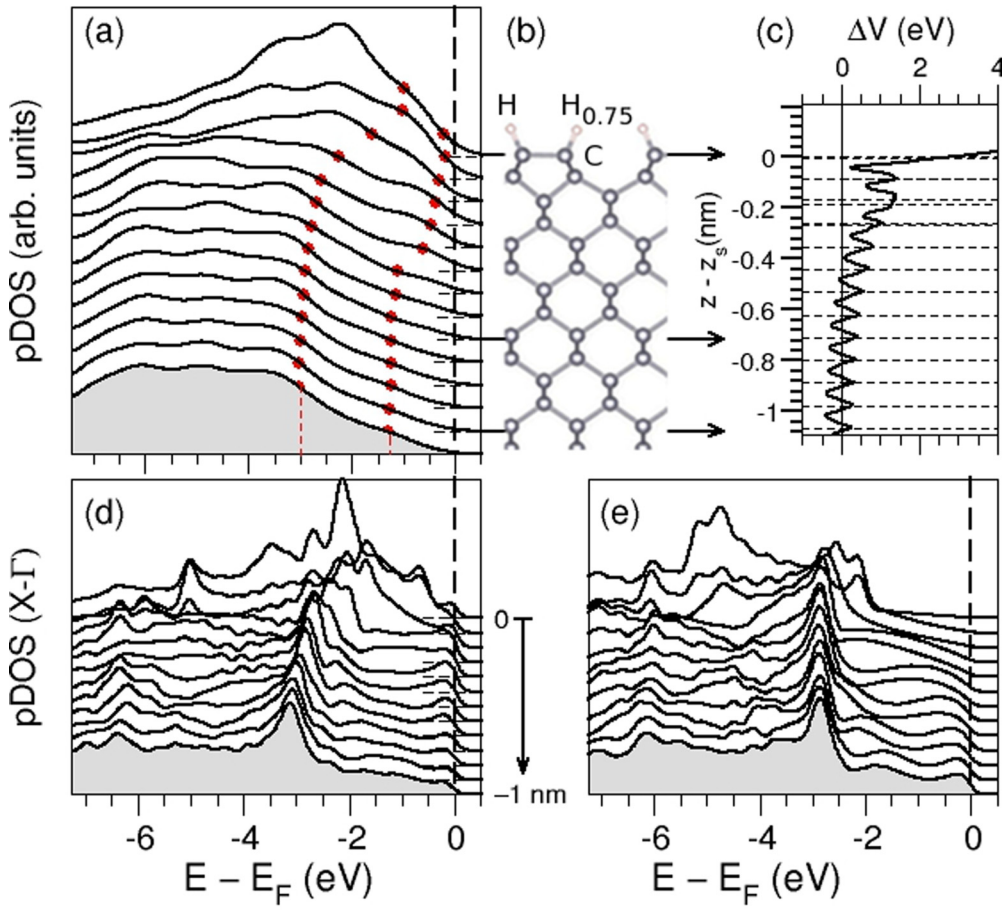

FIG. 2. (a) pDOS calculated on a $(4 \times 8 \times 1)$ k-point Monkhorst-Pack grid in the BZ and projected on C atoms at different distances from the surface as a function of energy. pDOS curves, except the bottom one, are offset vertically for clarity. The zero of the energy is the last occupied eigenvalue. Small red spheres mark energy values with same pDOS intensity. (b) Atomic structure of a portion of the supercell, with $\hat{z}$ axis along the [001] direction. Gray and white spheres denote C and H atoms, respectively. The position of the $H_{0.75}$ atom is indicated. (c) In-plane averaged local potential ΔV (eV) as a function of distance from the surface, $z - z_s$ (nm). The median value of its oscillation in the bulk portion of the supercell ($|z - z_s| \geqslant 0.7$ nm) is chosen as zero of the x axis. Horizontal arrows link selected pDOS in (a) to corresponding atomic positions in (b) and $z - z_s$ values in (c). (d) pDOS calculated for the $H_{0.75}$ supercell with a uniform grid of k points on the Γ-X direction. (e) pDOS for a HD supercell without the $H_{0.75}$ substitution on a uniform k-point grid along Γ-X.

symmetrical supercell with H atoms on both slab sides in the known dimer-reconstructed surface geometry obtained after atomic force relaxations [30]. One H atom per surface area is then substituted by a PAW/PBE pseudopotential, supplied with VASP, representing a hydrogenlike atom with effective atomic number Z=0.75 ($H_{0.75}$ hereafter), thereby modeling the effects of diamond surface acceptors. We mention here that there is no net charge in the supercell: $H_{0.75}$ is a device to only partially passivate the dangling bonds of the surface C atoms [31], keeping the system neutral. While the slab is about 6 nm long, the effect of the incomplete surface passivation mimicked by $H_{0.75}$ is completely screened at $\simeq$ 1 nm below the surface, as shown below. A portion of the supercell geometry is shown in Fig. 2(b).

Calculated ground-state DOS projected onto C atoms of different supercell layers (hence, pDOS) are reported in Fig. 2 [panel (a)] as a function of energy. The zero of the energy axis (E_F, Fermi energy of the calculations) is set to the last occupied valence band eigenvalue. The bottom gray-filled curve corresponds to the pDOS of a bulklike layer at distance $z - z_s \simeq 1$ nm from the surface. pDOS except the bottom one are offset vertically for clarity, and each curve is the average pDOS over the two C atoms per (2×1) layer. In the two bottom panels, pDOS are calculated as weighted sums over a uniform k-point grid along the Γ-X direction of the supercell Brillouin zone (BZ) for the $H_{0.75}$ supercell [left panel (d)] and for a structurally identical supercell without the $H_{0.75}$ substitution [right panel (e)].

We extract isovalues of the pDOS as a function of $z - z_s$ by choosing several pDOS intensity values along the bottom pDOS curve and recording their energy positions on all other layer-projected DOS. In panel (a), two sets of small red spheres mark the energy positions of two features close to E_F chosen to visualize a general behavior, i.e., an overall upward bending in energy as z approaches z_s. The upward bending is also evident when comparing pDOS on Γ-X [panels (d) and (e) of Fig. 2]. While the energy position of the main pDOS peak in Fig. 2(e) ($\simeq -3$ eV) does not change throughout all pDOS (except for the two topmost surface layers), in the $H_{0.75}$-supercell calculations [panel (d)], a progressive shift upward in energy is evident, taking place in a $\simeq$ 0.6-nm-wide region close to the surface. In the bulk portion of the $H_{0.75}$ supercell (for $|z| \geqslant 0.7$ nm), the peak position is instead constant. Moreover, a nonzero density of states at the Fermi energy, with a pronounced localization in the same surface region, is evident in panel (d), a feature that is absent in the calculated DOS of bare HD diamond on the right.

The in-plane-averaged local potential (ionic plus Coulomb contributions) as a function of the distance from the surface is shown in Fig. 2(c). It oscillates around a median value that is constant in the bulk portion of the supercell and increases in the vicinity of the surface. This behavior is in agreement with the building up of a charge depletion region in that region. That being so, although being aware that the band-structure details depend on the real potential acting on the surface and the specific adsorbate layer, we believe that the model adopted here catches up the main physical ingredients of the system: a spatially confined charge redistribution, an upward energy shift of the pDOS taking place a few layers below the surface, and an otherwise electronically unperturbed bulk portion.

The DFT electronic bands for the $H_{0.75}$ supercell have been unfolded into the Γ-X direction of diamond primitive Brillouin zone (p-BZ) with the procedure implemented in the BANDUP code [32]. The supercell band structure is calculated on a set of k points of the BZ chosen to unfold into selected $\mathbf{q}$ points of the p-BZ (here, $\mathbf{q} = q_{/\!/} \in [\Gamma]$-X) and unfolded spectral weights, $w_i(E,q_{/\!/})$, derived from the plane-wave expansion coefficients of the supercell eigenstates, can be directly compared to ARPES intensities. Figure 3(a) reports the calculated $w_i(E - E_F,q_{/\!/})$ on a color scale. Without inclusion of spin-orbit terms, the six p-like valence bands of diamonds are degenerate at Γ and disperse downwards along the Γ-X direction into two parabolic bands. This is reflected in the most intense calculated dispersion, which starts from the Γ states at $\simeq -0.2$ eV with the largest spectral weight, w_{max}, and reaches $E - E_F \simeq -2.5$ eV at $q_{/\!/} \simeq \pm 0.6$ Å^{-1}.

In addition to this dispersion, the unfolding procedure assigns nonzero spectral weights (roughly, 10% of w_{max}) to lower-intensity bands at Γ that cut the zero of the energy

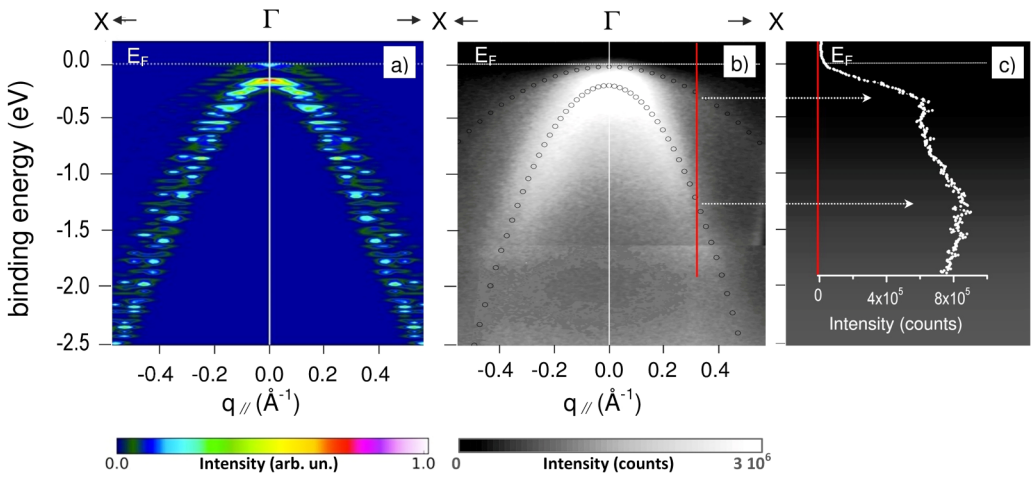

FIG. 3. (a) Spectral weights of theoretical bands unfolded on the X-Γ-X direction of diamond p-BZ on a color scale. (b) ARPES band structures along X-Γ-X measured on the AIR HD sample at 31-eV photon energy. (c) EDC at $q_{/\!/} = 0.3$ Å^{-1}.

axis. Their dispersion can be followed up to $q_{/\!/} \simeq \pm 0.3\,\text{Å}^{-1}$ and energy $E - E_F \simeq -0.25\,\text{eV}$, where the weights assigned by the unfolding procedure fade out. At variance with the high-intensity bands, they are distinctly spatially localized on C layers in a $\leqslant$ 1-nm-wide region from the surface layer, as is evident from their layer projections (not shown). It is then possible to assign an energy-momentum behavior to the electronic states that are partially occupied, spatially confined in a surface region and upward bent in energy, responsible for the akin pDOS features discussed above and reported in Figs. 2(a) and 2(d).

Theoretical results are compared to the ARPES-determined electronic structure in the momentum-energy space, for the conductive sample. A snapshot of the region close to E_F is reported in Fig. 3(b), showing parabolic band structure with negative concavity. The most intense band disperses from BE $= -0.2$ eV at Γ down to -2.7 eV at parallel momentum $q_{/\!/} = 0.54\,\text{Å}^{-1}$. These data well reproduce the dispersion of the theoretical bands with higher spectral weights. Energy resolution and lifetime broadening limitations prevent the observation of the expected band splitting. Close to E_F, ARPES features with lower intensities reveal bands with smaller curvature, resembling the corresponding calculated bands cutting E_F in the left panel. This finding is highlighted in Fig. 3(c), showing an energy distribution curve (EDC) at constant parallel momentum $q_{/\!/} = 0.3\,\text{Å}^{-1}$. Two structures in the spectrum can be resolved, at binding energies $\simeq -0.3$ eV and -1.25 eV, corresponding to the two bands visible in the ARPES data. We observe that the ratio of the experimental intensities at Γ is 1 : 10, close to what is found for the theoretical bands in Fig. 3(a).

In order to discriminate the surface/bulk character of the ARPES features, angle-integrated PES spectra (not shown here) have been measured around the normal emission direction for $h\nu = 31,26,21$ eV. The best data fit is compatible with a function given by the sum of two contributions: (i) one contribution due to the band close to the Fermi level, which does not disperse with $h\nu$; (ii) a broader contribution at deeper binding energy that disperses with $h\nu$. Notably, the reduced intensity for decreasing photon energy of the nondispersing peak close to the Fermi level can be due both to cross-section effects and to the increased probing depth (energy of 31 eV is nearby the minimum). These findings support the interpretation of the 2D character of the flatter band, whose momentum dispersion along the (001) direction, determined from the ARPES data measured at $h\nu = 31$ eV, is shown in Fig. 3(b).

ARPES provides also a direct determination of effective hole masses. A second-order polynomial fit of the most intense band dispersion, displayed by open circles in Fig. 3, gives a hole mass $m_h = (0.43 \pm 0.02)\,m_0$, where m_0 is the electron rest mass. In the fitting procedure, the experimental points are statistically weighted with the inverse of their intensity, hence higher-intensity data around Γ have larger weight than lower-intensity data at deeper BE, where the fit might look imperfect. The error tolerance derives from the choice of the datasets used to fit the band in the vicinity of its apex: the two extreme values for m_h have been obtained by including experimental points with intensity higher than 60% and 85% of the maximum, respectively. Our determination of m_h favorably compares with the average one-band value determined by ARPES in normal emission experiments on hydrogen-terminated diamond [33], $m_h = (0.39 \pm 0.30)\,m_0$, as well as with the light-hole mass measured along the Γ-X direction in heavily doped diamond [19], $m_{lh}^{100} = (0.417{-}0.408)m_0$.

Fitting the ARPES data in the Fermi region results in the flatter curve displayed in Fig. 3, with a corresponding larger effective mass, $m_{hs} = (2.2 \pm 0.9)\,m_0$. Comparing theoretical data to the experimental fit, we find a reasonable agreement of the DFT and ARPES downwards dispersion in the energy-momentum region ($\Delta q_{/\!/} \simeq \pm 0.3\,\text{Å}^{-1}$, $\Delta(E - E_F) \simeq -0.25\,\text{eV}$) used to define the parabolic fit function and thus the effective mass.

The determination of effective masses of holes in a HD conducting layer has been recently addressed [16,18,34]. Indirect measurements of two-dimensional HD hole effective masses have been derived by Takahide *et al.* [34] from the temperature dependence of Shubnikov–de Haas oscillations at HD (111) surfaces. They found masses close to the cyclotron masses of the diamond valence bands. There are reasons to be cautious of a direct comparison with our (and Edmonds *et al.*'s [16,18]) results. The main reason is the experimental setup: holes are injected in the sample by embedding it in an operating electric double-layer transistor; the main issues here is, as the authors themselves point out, that carrier density and mobility may be strongly inhomogeneous due to device architecture (involving an ionic liquid interfacing the HD to the gate oxide). Another issue is that masses are attributed to oscillations at relatively low characteristic fields. It may be that Fermi surface sections with larger area and effective mass, and smaller occupation (such as ours), may not be revealed clearly in this observation range or may be swamped out by stronger signals.

Numerical estimates of 2D masses can be obtained from the two-dimensional hole density of states as a function of energy in a $\mathbf{k} \cdot \mathbf{p}$ framework, thus accounting for band nonparabolicity and anisotropy. A crucial ingredient of this formalism is the Luttinger parameters γ_i of bulk diamond valence-band maxima. Edmonds *et al.* first used [16] a calculated set of parameters [35] and came up with 2D masses close to bulk diamond masses (in a range 0.31–0.57 m_0). In a recent study [18], instead they used the latest γ_i's provided by cyclotron resonance [36] and obtained a 2D light-hole mass of 1.9 m_0, in close agreement with our direct measurement.

In summary, by correlating conductance experiments and photoemission spectroscopy with the support of a theoretical model capable of mimicking charge uptake by surface acceptors, we have unambiguously determined the electronic structure of a hole gas confined in the near-surface topmost layers of conductive HD. By using a consolidated procedure to switch on and off the air-induced surface conductivity in a reproducible way, we have shown that in air-exposed (100) surfaces, carriers are organized in a twofold band structure dispersing along the Γ-X direction in the momentum space, with effective masses less than half and about twice that of the electron rest mass, respectively. The surface sensitivity of our PES experiments, performed at energy close to the minimum of the electron probing depth, and the comparison of measured

data with DFT unfolded bands and pDOS characteristics, give us enough confidence to identify the low-intensity bands as spatially confined electronic states arising from the buildup of a charged-depleted surface region.

The question of which adsorbed molecular species is responsible for the surface charge transfer, although addressed by several works, still awaits a conclusive answer. Carefully tuned experiments, able to characterize samples exposed to selected molecular gases, are yet needed, as well as extensive *ab initio* calculations able to overcome well-known DFT criticality in accounting for relative alignment of semiconductor band-edge states and localized molecular levels. Nevertheless, the outcomes of this work provide a robust picture of the electronic structure responsible for the HD surface conductivity by shedding light at a microscopical level on the results obtained by conductivity measurements performed by surface contact methods.

This work was partially supported by European Union's Seventh Framework Programme for research, technological development and demonstration, under Grant Agreement No. 308975 (ProME^{3}ThE^{2}US^2, http://www.prometheus-energy.eu). S.I and F.O. are grateful to the Elettra support for synchrotron radiation users activity. Authors are indebted to S. Nannarone and V. Fiorentini for valuable discussion and to G. Stefani for critical reading of the manuscript.

[1] K. Sun, Nat. Mater. **14**, 262 (2015).
[2] N. Savage, Nature (London) **519**, S7 (2015).
[3] X. Cui, C. Wang, A. Argondizzo, S. Garrett-Roe, B. Gumhalter, and H. Petek, Nat. Phys. **10**, 505 (2014).
[4] K. L. Krycka, J. A. Borchers, R. A. Booth, Y. Ijiri, K. Hasz, J. J. Rhyne, and S. A. Majetich, Phys. Rev. Lett. **113**, 147203 (2014).
[5] C. J. H. Wort and R. S. Balmer, Mater. Today **11**, 22 (2008).
[6] C. E. Nebel, B. Rezek, D. Shin, H. Uetsuka, and N. Yang, J. Phys. D: Appl. Phys. **40**, 6443 (2007).
[7] T. Sun, F. A. M. Koeck, C. Zhu, and R. J. Nemanich, Appl. Phys. Lett. **99**, 202101 (2011).
[8] P. Calvani, A. Bellucci, M. Girolami, S. Orlando, V. Valentini, A. Lettino, and D. M. Trucchi, Appl. Phys. A **117**, 25 (2014).
[9] F. Maier, M. Riedel, B. Mantel, J. Ristein, and L. Ley, Phys. Rev. Lett. **85**, 3472 (2000).
[10] P. Calvani, A. Corsaro, M. Girolami, F. Sinisia, D. M. Trucchi, M. C. Rossi, G. Conte, S. Carta, E. Giovine, S. Lavanga, E. Limiti, and V. Ralchenko, Diamond Relat. Mater. **18**, 786 (2009); V. Camarchia, F. Cappelluti, G. Ghione, M. C. Rossi, P. Calvani, G. Conte, B. Pasciuto, E. Limiti, D. Dominijanni, and E. Giovine, Solid-State Electron. **55**, 19 (2011).
[11] D. Takeuchi, M. Riedel, J. Ristein, and L. Ley, Phys. Rev. B **68**, 041304 (2003).
[12] V. Chakrapani, J. C. Angus, A. B. Anderson, S. D. Wolter, B. R. Stoner, and G. U. Sumanasekera, Science **318**, 1424 (2007).
[13] W. Chen, D. Qi, X. Gao, and A. T. S. Wee, Prog. Surf. Sci. **84**, 279 (2009).
[14] Moritz V. Hauf, P. Simon, M. Seifert, A. W. Holleitner, M. Stutzmann, and Jose A. Garrido, Phys. Rev. B **89**, 115426 (2014).
[15] M. Kubovic, M. Kasu, and H. Kageshima, Appl. Phys. Lett. **96**, 052101 (2010); Jpn. J. Appl. Phys. **49**, 110208 (2010).
[16] M. T. Edmonds, C. I. Pakes, and L. Ley, Phys. Rev. B **81**, 085314 (2010).
[17] M. T. Edmonds, M. Wanke, A. Tadich, H. M. Vulling, K. J. Rietwyk, P. L. Sharp, C. B. Stark, Y. Smets, A. Schenk, Q.-H. Wu, L. Ley, and C. I. Pakes, J. Chem. Phys. **136**, 124701 (2012).
[18] M. T. Edmonds, L. H. Willems van Beveren, O. Klochan, J. Cervenka, K. Ganesan, S. Prawer, L. Ley, A. R. Hamilton, and C. I. Pakes, Nano Lett. **15**, 16 (2015).
[19] H. Guyot, P. Achatz, A. Nicolaou, P. Le Fèvre, F. Bertran, A. Taleb-Ibrahimi, and E. Bustarret, Phys. Rev. B **92**, 045135 (2015).
[20] B. Ziaja, R. A. London, and J. Hajdu, J. Appl. Phys. **99**, 033514 (2006).
[21] K. H. L. Zhang, R. G. Egdell, F. Offi, S. Iacobucci, L. Petaccia, S. Gorovikov, and P. D. C. King, Phys. Rev. Lett. **110**, 056803 (2013).
[22] F. Offi, S. Iacobucci, P. Vilmercati, A. Rizzo, A. Goldoni, M. Sacchi, and G. Panaccione, Phys. Rev. B **77**, 201101(R) (2008).
[23] P. E. Blöchl, Phys. Rev. B **50**, 17953 (1994); G. Kresse and D. Joubert, *ibid.* **59**, 1758 (1999).
[24] J. P. Perdew, K. Burke, and M. Ernzerhof, Phys. Rev. Lett. **77**, 3865 (1996).
[25] G. Kresse and J. Hafner, Phys. Rev. B **47**, 558 (1993); G. Kresse and J. Furthmüller, Comput. Mater. Sci. **6**, 15 (1996); Phys. Rev. B **54**, 11169 (1996).
[26] S. Kaciulis, A. Mezzi, P. Calvani, and D. M. Trucchi, Surf. Interface Anal. **46**, 966 (2014).
[27] L. Petaccia, P. Vilmercati, S. Gorovikov, M. Barnaba, A. Bianco, D. Cocco, C. Masciovecchio, and A. Goldoni, Nucl. Instrum. Methods Phys. Res., Sect. A **606**, 780 (2009).
[28] C. E. Nebel, N. Yang, H. Uetsuka, T. Yamada, and H. Watanabe, J. Appl. Phys. **103**, 013712 (2008).
[29] Y. M. Wang, K. W. Wong, S. T. Lee, M. Nishitani-Gamo, I. Sakaguchi, K. P. Loh, and T. Ando, Phys. Rev. B **59**, 10347 (1999).
[30] Calculations are performed at cutoff energy of 450 eV, with a $4 \times 8 \times 1$ Monkhorst-Pack grid for k-point summation, at fixed PBE equilibrium in-plane lattice constant $a_0 = 3.57$ Å. The length of the vacuum space is 15 Å. Convergence criteria on total energy (E_{tot}) and atomic force components (F_i) are $\Delta E_{\text{tot}} \leqslant 0.1$ meV and $\Delta F_i \leqslant 0.02$eV/Å, respectively. In the pDOS integrals, a Gaussian smearing with $\sigma = 0.15$eV was used.
[31] L.-W. Wang and J. Li, Phys. Rev. B **69**, 153302 (2004).
[32] P. V. C. Medeiros, S. Stafström, and J. Björk, Phys. Rev. B **89**, 041407(R) (2014); P. V. C. Medeiros, S. S. Tsirkin, S. Stafström, and J. Björk, *ibid.* **91**, 041116(R) (2015).
[33] M. T. Edmonds, A. Tadich, M. Wanke, K. M. ODonnell, Y. Smets, K. J. Rietwyk, J. D. Riley, C. I. Pakes, and L. Ley, Phys. Rev. B **87**, 085123 (2013).
[34] Y. Takahide, H. Okazaki, K. Deguchi, S. Uji, H. Takeya, Y. Takano, H. Tsuboi, and H. Kawarada, Phys. Rev. B **89**, 235304 (2014).
[35] M. Willatzen, M. Cardona, and N. E. Christensen, Phys. Rev. B **50**, 18054 (1994).
[36] N. Naka, K. Fukai, Y. Handa, and I. Akimoto, Phys. Rev. B **88**, 035205 (2013).